

Active nanoceramic compound dipped in biopolymers to create composite coating for metallic implant surface

Amjed Al-Khateeb^{*}, Emad S. Al-Hassani, Akram R. Jabur

Department of Materials Engineering, University of Technology, Iraq, Baghdad

ARTICLE INFO

Keywords:

Biofunctionalization
Electrospinning
Nanofiber
Piezoelectric
Dielectric constant

ABSTRACT

Biofunctionalization of an implant using functional ceramics with exceptional electrical characterization, such as BaTiO₃ and SrTiO₃, has gained considerable attention in creating a composite coating with bio-polymer to activate metal implant surfaces for bone tissue engineering applications and, at the same time, resist bacterial infection. A Ti–Zr alloy sample was created by powder technology, and then a coating was applied using the electrospinning technique. Individually, nanopowders of ceramic compounds such as nBaTiO₃ and nSrTiO₃ were added to a blend of polycaprolactone and chitosan to create composite solutions that could be converted into a nanofibrous coating layer using the electrospinning technique. The samples were analyzed for their morphology, chemical composition, surface roughness, dielectric constant, and wettability. The techniques employed were SEM, EDS, FTIR, an LCR meter, and a contact angle goniometer. The samples' cytocompatibility was assessed by examining the cell viability, ALP activity, proliferation, and attachment of MC3T3-E1 osteoblast cells on both coated and uncoated sample surfaces. The bacterial resistance assays were conducted against *Staphylococcus aureus* and *Streptococcus mutans*. The findings demonstrate a notable enhancement in the biocompatibility of the coated specimens following a week of cellular cultivation. The composite coating containing piezoelectric BaTiO₃ has a dielectric constant ϵ_r (16) close to dry human bone at 100Hz frequency. Cell proliferation increases dramatically with time in coated samples, and the improvement approaches 125.16% for (BA1) and 111.38% for (SR1) as compared to uncoated Ti–25Zr sample. Cell viability percentage for the coated samples is compared with bare Ti–25Zr, which has an $80.52 \pm 1.97\%$ crucial increase, while (BA1) has 181.63 ± 17.87 and (SR1) $170.09 \pm 18.12\%$. No zone of inhibition was detected in the bacterial resistance test for the uncoated sample, while the samples with composite coating show an adequate and comparable inhibitory zone. The composite nano-fiber has a strong biocompatibility, and the coating process is simple and economical, holding potential for use in orthodontic and orthopedic bone regeneration applications.

1. Introduction

Bone possesses an intricate structure, and bone defect recovery is especially difficult because of the diverse cell types and its mechanical characteristics. The inability of the body to cure a large-volume bone lesion presents further difficulty [1]. The therapeutic

^{*} Corresponding author.

E-mail address: mae.19.07@grad.uotechnology.edu.iq (A. Al-Khateeb).

<https://doi.org/10.1016/j.heliyon.2023.e19594>

Received 21 March 2023; Received in revised form 23 August 2023; Accepted 28 August 2023

Available online 4 September 2023

2405-8440/© 2023 The Authors. Published by Elsevier Ltd. This is an open access article under the CC BY-NC-ND license (<http://creativecommons.org/licenses/by-nc-nd/4.0/>).

benefits of the two most prevalent procedures for bone regeneration, autologous bone transplant and bone allograft, can not be assured because patient complications and mortality are common. As a result, research into alternative bone substitutes continues to be crucial and important [2,3].

The development of biomaterials that can treat bone ailments has increased notably over the past few years. The need to replace native bone with a suitable multifunctional biomaterial is one of the main reasons for its development [4].

Metallic implants, especially those made from titanium and its alloys, are the most commonly utilized biomaterials in orthopedic and dental procedures. This is primarily because these implants have desirable mechanical qualities, resistance to corrosion, and favorable biocompatibility in the live body [5,6]. Nevertheless, there are still specific issues that need to be resolved. Because of the inert surface of these alloys, one of the main challenges is the insufficient integration of the materials with the natural tissue around them. An implant material's poor biointegration is frequently linked to unsatisfactory long-term medical results [7–9].

Researchers have recently shifted their attention to active layers with electrical polarization that can enhance the biological efficacy of the coatings. These advanced coatings promote bone cell growth using non-linear electrical characteristics, including piezoelectricity, ferroelectricity, and dielectric constant (ϵ_r). Additionally, these electrically active layers are crafted to support electrical stimulation of cells, triggering specific cellular reactions, like the proliferation of osteoblasts in bone graft implants [10,11].

Piezoelectric materials have attracted much interest in the area of bone tissue engineering because they can be used to stimulate bone growth with electricity. The number of smart nanocomposites made of biocompatible, functional, and non-toxic materials used in biomedical applications has grown. Piezopolymers are needed to fix living tissues like skin, bone, cartilage, tendons, and the heart. In this way, ceramic nanoparticles having piezoelectric capabilities are combined with polymer matrices, and the resulting hybrid materials hold promise for diverse biomedical uses. This is because nanomaterials have a much more reactive surface area than micro or macroparticles, which makes it easier for them to react chemically with a biological medium. Furthermore, The fibrous components in all connective tissues, such as keratin, collagen, fibrin, reticulum, elastin, and cellulose structures, give them piezoelectric characteristics. These tissues' generating piezoelectric potential is essential for cell adhesion and growth [3,10].

In the field of bone tissue engineering, piezoelectric ceramics, especially barium titanite (BaTiO_3), have gotten a lot of attention because they are biocompatible, can keep a charged surface, and help bone cells stick together and grow. The ferroelectric perovskite oxide barium titanate, BaTiO_3 , is regarded as a smart material since it exhibits piezoelectric capabilities by generating electric polarization when subjected to minor structural distortions. Several claims have been made about the biological features of BTO, including its biocompatibility with cells. Because of this, it is viewed as a substance with great potential for use in biomaterial applications [12–14].

Strontium Titanate (SrTiO_3 , ST) is a perovskite that has been extensively investigated for utilized in varistors, as fuel cell anodes, and for various further relevant advantages. SrTiO_3 with paraelectric characteristics is typically the most favored addition to a composite due to its exceptionally high dielectric constant (ϵ_r) values [15]. The majority of the strontium present in human bodies, approximately 98%, is located within the bone tissue, where it helps to improve bone metabolism by promoting bone growth and inhibiting the resorption of bone. Sr has been found to be a potential agent for treating bone disorders, and strontium ranelate, for instance, has been utilized in clinics for decades [16].

However, these ceramic materials' brittleness and poor processability prevent their manufacture and common use. One of the most suggested methods for overcoming this limitation involves adding the active ceramic component to the polymer as filler to create a composite multifunctional coat.

Polycaprolactone (PCL) was chosen as the dispersion phase because of its low melting point, ease of processing, and widespread applicability in bone tissue engineering [13,17]. Chitin deacetylation produces the polymer known as chitosan (CS). CS is a natural polymer known for its impressive absorption ability, biodegradability, and compatibility with biological systems. It is also antimicrobial. As CS interacts with the tissue of the host, its interaction with different cellular activities related to wound healing can expedite the recovery process [10,18]. Thus, PCL/Chitosan combined for the coating procedure is preferable to employing than using two ingredients separately to improve biological and mechanical performance [19].

In this study, a multifunctional composite coat was prepared to activate the inert surface of the Ti–Zr alloy. Bioactive nano-ceramic compounds such as ferroelectric barium titanate (BaTiO_3), which has piezoelectric characteristics, and perovskite Strontium Titanate (SrTiO_3) that display substantially high (ϵ_r) were used. These ceramic compounds were individually added to PCL/Chitosan blended polymer as filler material to form a composite solution and applied as nanocomposite fiber using the electrospinning method on Ti–Zr alloy surface. Coated and non-coated specimens were examined using FTIR, SEM, EDS, and contact angle. The bacterial inhibition zone was also tested. Cytotoxicity of the coated and uncoated samples were evaluated invitro.

2. Experimental

2.1. Chemicals

Ti-powder (99.7 purity, APS 150–200 μm , Sigma Aldrich, USA), Zr-powder (99.5 purity, APS 100–150 μm , Sigma Aldrich USA), Nano-Chitosan powder (80-nm APS, intermediate molecular mass, deacetylated to 90%) was supplied by (International Hongwu Group, China). PCL ($M_n = 8 \times 10^4$ sigma Aldrich, USA), nanoceramic (BaTiO_3 , SrTiO_3) both (APS 80–100 nm) obtained from (Chemical Industry Jinan Boss, China), All of the acetone, Sulfuric acid, hydrochloric acid, formic acid, and acetic acid that were used in this study came by (Thomas Baker chemical company, India) and where each component is of analytical-grade quality.

2.2. Metallic sample creation

This study prepared Ti–Zr alloy using powder metallurgy in cylindrical disc shape samples with dimensions (15 mm diameter, 2 mm height). Titanium powder was combined for 6 h with 25 wt% zirconium powder before being compressed at 500 MPa. Then vacuumed furnace at 10^{-3} torr was used to sinter green compact disc at a heating rate of $10^{\circ}\text{C}/\text{min}$, a dwell time of 2 h at 1300°C , and then allowed to cool inside the furnace slowly.

2.3. Substrate sample surface treatment

The sintered Ti–25Zr alloy was polished manually using silicon carbide paper with grits from 120 to 1000. The samples underwent a cleaning process with acetone followed by deionized water in an ultrasonic cleaner for a duration of 20 min. The implant's surface was made more active and had micro and nano roughness by treating it in a mixture of sulfuric acid, hydrochloric acid, and water was used in a 1:1:1 ratio at 60°C for 1 h. Furthermore, the specimens were subjected to a treatment in 10 M Sodium hydroxide (NaOH) treatment at 60°C for a day and then dried for a night.

2.4. Porosity evaluation

Ti–25Zr sintered alloys were examined to calculate porosity percentage by an Eq. (1):

$$p = 1 - \frac{\rho}{\rho_0} \times 100\% \quad (1)$$

where ρ : the alloy's apparent density, determined using the liquid displacement technique based on Archimedes' principle. ρ_0 represents the standard theoretical density of the related alloy, computed by Eq. (2):

$$\rho_0 = \frac{1}{\left(\frac{C\%}{\rho_C}\right) + \left(\frac{D\%}{\rho_D}\right)} \quad (2)$$

where C% and D%: are the element's mass fractions of C and D, ρ_C and ρ_D are the theoretical densities of materials C and D, respectively.

2.5. Mechanical properties of the substrate sample

The samples' hardness was assessed utilizing an HVS-1000 Vickers microhardness instrument from Laryee Technologies in China. The load applied to the indenter was 9.8 N, and the dwell time was 15 s. The mean microhardness values were determined based on local measurements from 10 different locations. The compressive strength was measured at ambient temperature using the Brazilian method on a sample with dimensions (15 mm diameter and 18 mm height) (computer control universal testing machine built in China by Instron). Finally, the modulus of elasticity was determined utilizing (Ultrasonic CCT-4 Tester, U.K) and the subsequent Eqs. (3) and (4):

$$\nu = 1 - \frac{1}{2} \cdot \frac{1}{1 - (C_{\text{trans}}/C_{\text{long}})^2} \quad (3)$$

$$E = 2 \cdot \rho \cdot (1 + \nu) C_{\text{trans}}^2 \quad (4)$$

In this context, C_{trans} refers to the speed of transverse waves, C_{long} represents the speed of longitudinal waves, ν is the symbol for the Poisson ratio, while E stands for the modulus of elasticity, and ρ represents the material density.

2.6. Microstructural and chemical examination for base sample

An X-ray diffractometer utilizing Cu K α radiation, operating at 40 kV and 40 mA in room temperature conditions, was employed to determine the crystalline phase (XRD, 6000 Shimadzu, Japan). The surface topography and microstructures of the samples were examined using scanning electron microscopy (SEM, TESCAN VEGA3, Czech Republic). Energy-dispersive spectroscopy (EDS), which effectively combines SEM imaging with elemental composition analysis, was employed to investigate the composition and uniformity of the sintered sample.

2.7. Electrospinning solutions preparation

To make chitosan (CS) solution, 2% (weight/volume) chitosan was added to 4/6 acetic/formic acid (vol/vol) (100 ml) and stirred for 12 h at 50°C using a hot plate magnetic stirrer until we got a clear solution. Polycaprolactone 8% (weight/volume) (PCL) was merged with the CS solution and agitated for Three hours until a clear and homogeneous PCL/CS blended solution was obtained. The Nano-BaTiO $_3$ and Nano-SrTiO $_3$ were added separately at 1% (weight/volume) each and agitated for 1 h to generate two solutions. The

PCL/CS/nBaTiO₃(BA1) and PCL/CS/nSrTiO₃(SR1) solutions were then homogenized for 3 min with a homogenizer (Ultrasonic Homogenizer, Model 300VT USA) to get them ready to be coated by electrospinning.

2.8. Electrospinning procedure

The solutions were filled into a 5-ml syringe that had a blunt-end 22 G gauge needle. The liquid was released with a flow rate of 1 ml/h through an infusion pump (Kd scientific 200 syringe pump from the USA). The tip of the needle was kept 10 cm away from the grounded sample. The needle was exposed to a controlling 20 kV voltage. The room's relative humidity ranged from 35 to 55%. Before an examination, the fibers were dehydrated in a desiccator overnight.

2.9. Electrospun coating fiber characterization

The microstructure and cross-section of gold-sputtered electrospun fibers were studied using secondary electrons (SE) generated by (FESEM) a field emission scanning electron microscope (InspectTM F50, Spain) operating at 15 kV. The resulting fibers' diameters and porosity were measured randomly on each fiber and analyzed using (ImageJ) Java-based image processing program. A dispersive energy X-ray (EDS) was utilized to verify the existence of Nano (BaTiO₃, SrTiO₃) in the PCL/CS blended polymer.

2.10. Mechanical strength and adhesion of electrospun coating fiber

The hardness of the coating layers was measured using a Vickers microhardness electronic device (HVS-1000, Laryee Technologies, China), applying a load of 0.098 N and a dwell length of 25s. The average microhardness values were determined by collecting local data from five sites. In contrast, the adhesion strengths of the composite coating films on Ti-25Zr substrates were assessed using a scratch test conducted on an auto scratch coating tester (WS-2005, China). A consistent force within the 1–2 N range was exerted, accompanied by a 6 mm/min sliding velocity, under ambient temperature conditions. Three replicates were conducted for each sample.

2.11. Electrical properties of coating

For electrical measurements, electrical capacity was analyzed using an LCR meter (UT612, UNI-T Hong Kong) that facilitate the frequency variation in range (100HZ – 100KHZ). The equation (Eq. 5) was employed to compute the dielectric constant at the specified five frequency points.

$$\epsilon_r = \frac{C \times d}{\epsilon_0 \times A} \quad (5)$$

where ϵ_r is the dielectric constant, ϵ_0 stands for 8.85×10^{-12} , C: represents the capacitance, A: denotes the surface area of the capacitor, and d: is the thickness of the composite layer.

2.12. Fourier transform infrared (FTIR) spectrometry

The chemical functional groups were investigated using FTIR test according to (ASTM E1252) with (Bruker Tensor 27 IR, Germany). The test was performed in the air after the specimen was placed into the instrument. Fourier transform investigations were carried out for pure (polycaprolactone, chitosan, BaTiO₃, SrTiO₃, and prepared composites coating) and were captured in range (4000–500) cm⁻¹ sectors.

2.13. Wettability test

Use of the sessile drop method with distilled water was employed to examine the wettability of the coated and non-coated samples (Optical contact angle SL200KS, China). The surface was subjected to a test where a droplet of pure water (1 µl) was placed on it and allowed to remain for a duration of 10 s, followed by measuring the contact angle. The wettability of a sample was determined by measuring the contact angle in triplicate with a camera-based contact angle instrument.

2.14. Antibacterial evaluation

The antibacterial potential of the prepared (PCL/CS/nBaTiO₃, PCL/CS/nSrTiO₃) nano-composite fibers and non-coated sample was assessed using the Inhibition Zone technique. The bacteria Model microorganisms included *Streptococcus mutans* (Strp. mutans) and *Staphylococcus aureus* (S. aureus). The agar plates enriched with nutrients had 1 mL of a solution that contained bacteria at approximately 10⁸ CFU/mL was used to infect the specimens using the spread plate method. After applying the nanofiber coating, the substrate in the form of a circular layer measuring 1.5 cm in diameter to the inoculation plates, they were kept inside an incubator set to a temperature of 37 °C for 24 h. Each electrospun nanofiber sample's clear area was used to compute the inhibition zones.

2.15. *In vitro* cytocompatibility evaluation

2.15.1. Purification of samples

Prior to cell culture, samples were sterilized using UV light over a period of 20 min, immersed for 1 h in 75% ethanol, then washed at least three times with PBS for 15 min each.

2.15.2. Culture of cells

The Pasteur Institute was the source for the cell line type MC3T3-E1 (Tehran, Iran). The cell lines were kept in Dulbecco's Modified Eagle Medium (DMEM; Gibco, Life Technologies, Waltham, MA, USA), supplemented with 10% fetal bovine serum (FBS; BioWest SAS, Nuaille, France) and 1% PSF (antibiotic antimycotic solution, Sigma-Aldrich®, St. Louis, MO, USA), in a humidified incubator with 5% CO₂ in air at 37 °C. Upon reaching 75% confluence, the cells were dissociated using a solution of phosphate-buffered saline (PBS) supplemented with 0.25% trypsin at a temperature of 37 °C (Gibco, Invitrogen, Waltham, MA, USA) and 0.1% ethylenediaminetetraacetic acid (Merck, Darmstadt, Germany). Subsequently, the cells were resuspended in Dulbecco's Modified Eagle Medium (DMEM) supplemented with 10% fetal bovine serum (FBS) and 1% penicillin-streptomycin-fungizone (PSF).

2.15.3. Cells seeding

The cell suspension was evenly spread across the samples by gently adding five 40 µl drops; the cells were distributed into 24-well culture dishes with a concentration of 10,000 cells in each well. Afterward, the cell/sample complexes were exposed to the medium following a 30-min attachment phase.

2.15.4. Cell viability

The cell viability of coated and uncoated surfaces was evaluated utilizing AlamarBlue test (Sigma-Aldrich, St. Louis, MO, USA). In brief, each well was incubated with 1 ml of AlamarBlue solution at 10% (v/v) for about 4 h. Subsequently, an ELISA Reader (Stat Fax-2100, Miami, FL, USA) was used to measure the absorbance at 530/560 nm. Cell viability was calculated on days 1, 3, and 7 by dividing the absorbance of the sample by the absorbance of the control. Three independent experiments (n = 3) yielded data.

2.15.5. Cell proliferation

The proliferation of pre-osteoblast cells (MC3T3-E1) was estimated by counting the cells in the samples on days 1, 3, and 7, as well as by employing the AlamarBlue® fluorescent test. At every designated interval, samples were moved to a fresh plate, and after adding AlamarBlue®, the fluorescence was recorded. Samples were processed through the AlamarBlue® test daily, rinsed twice using PBS, and subsequently kept in a humidified incubator with 5% CO₂ at 37 °C for osteoblast cultivation. Information was compiled from independent triplicated experiments on the samples (n = 3).

2.15.6. Alkaline phosphate (ALP) activity

An essential technique for determining osteogenesis differentiation is the alkaline phosphatase (ALP) assay. On coated and uncoated samples, alkaline phosphatase (ALP) activity of MC3T3-E1 pre-osteoblasts was measured to determine their osteoblastic phenotype. Cell lysis was performed using Milli-Q water, followed by three cycles of freeze-thawing. During the cell culture period, on days 3 and 7, the ALP activity on the surface of the sample was examined to evaluate its behavior. The protein content-nitrophenyl-phosphate substrate (Merck, Darmstadt, Germany) was employed for the analysis of ALP, at a pH of 10.3, following established procedures [20]. A spectrophotometer (BioTek, Winooski, VT) was used to instantly measure the plate at 405 nm to measure the absorbance related to the expression of (pNPP). The activity of alkaline phosphatase (ALP) was approximated by calculating the ratio of *para*-nitrophenyl phosphate to the protein amount. The findings were presented using a fold Change Formula compared to the permitted control.

2.15.7. Cell morphology

After seven days of cell seeding on both coated and uncoated samples, scanning electron microscopy (SEM) was utilized to analyze the cellular structures on their surfaces. On day 7, the cells that were treated with drugs were immobilized using a 4% glutaraldehyde solution. Subsequently, the cells were dehydrated using a succession of ethanol concentrations (50%, 70%, 80%, 90%, and 100%), each lasting 3 min. Finally, the cells were dried at ambient temperature. The seeded cells were subjected to gold coating employing (Edwards Sputter Burgess Hill Coater S150B from, U.K). Subsequently, the cells were seen via a scanning electron microscope (Zeiss EVO LS-15 from Oberkochen, Germany) with an accelerating voltage of 20 kV.

2.16. Statistical analysis

Originpro2023 was used to analyze the data (Northampton, Massachusetts, USA). Data is shown as mean ± standard deviation. One-way ANOVA and the Bonferroni method were used to compare the groups. Significant results were shown at the P < 0.05 confidence level.

3. Results and discussion

3.1. Characterization of phase and microstructure

The phase compositions of the alloy produced were determined utilizing X-ray diffraction analysis (XRD). The Ti–25Zr alloy's typical XRD profile is seen in (Fig. 1 a). The XRD findings indicated that the hcp α phase was the main phase of Ti–25Zr alloy. The Ti and Zr system has a complete solid solution that could clarify the reason why Ti–25Zr alloys demonstrate the presence of the α phase, as observed through optical microscopy (Fig. 1 b).

Furthermore, because Zr possesses a greater atomic radius (1.62 \AA) than Ti (1.47 \AA), The phase lattice parameters increase when Zr is added, which makes the peaks on the XRD chart move to a smaller angle. This observation is consistent with previous findings [21, 22].

The energy-dispersive X-ray spectroscopy (EDS) technique was utilized to examine the chemical composition and uniformity of the sintered samples (Fig. 2). shows the semi-quantitative chemical analysis results obtained by (EDS). The EDS analysis indicated the powder's homogeneity and purity, implying the absence of any additional elements, and revealed the proportions of the ingredients, demonstrating the proper mixing method.

3.2. Surfaces treatment

The Ti–25Zr samples chemically treated and untreated surfaces showed visible morphological variations. The surface of the base sample had ground grooves that acted as a baseline for comparison (Fig. 3a). Once the grooves had been etched with acid and alkali, they were clearly visible (Fig. 3b). The pit (Fig. 3c) also appeared to deepen and become more acute after treatment (Fig. 3d). The chemically altered surface is rougher with micro, nano-roughness, porosity, and more energy, enhancing the wetting properties of the surface and promoting better adhesion of the coating layer.

3.3. Mechanical and physical properties

Ti–25Zr's microhardness, tensile strength, compressive strength, elongation, porosity, and density are all detailed in. (Table 1).

As previously stated, the influence of Zr concentration on the mechanical characteristics of Ti–25Zr alloys was to improve all mechanical parameters over commercially Pure titanium [23,24]. Because Zr substitution caused impeded dislocation motion and deformed the crystal lattice, The hardness of Ti–25Zr alloys rises as the Zr content increases [21,24]. In addition, the complete solid solutions of Ti–25Zr alloys improved hardness, which was most likely caused by α phase solid solution hardening as well as the role of microstructure refinement [25].

Yet, adding Zirconium to a Ti improves its strength, but Zr concentrations beyond 25 wt% inhibit calcium phosphate synthesis, the main constituent of natural bones [26,27]. Also, high Zr concentrations must be cautiously approached because of increased proneness to experience pitting corrosion [28].

The alloy's strength in compression and tension is greatly enhanced by adding a small amount of Zr [21]. Probably, two causes contributed to the enhancement of tension and compression strength generated through alloying. The phase diagram demonstrates the absence of intermetallic compounds inside the α phase in the Ti–25Zr alloy. This implies that the mechanism of the solid solution introduces additional barriers to the slip system, enhancing its mechanical characteristics. Also, the Hall-Petch equation shows that alloy yield strength is increased by fine-grain strengthening. As Zr rose, the starting temperature of the phase transition fell, preventing phase growth. Increased the area of grain boundary due to grain refinement improved resistance to dislocation motion and enhanced qualities [29].

The main cause of aseptic deterioration in long-term service is stress shielding, which is a common problem in clinical cases. This happens when the bone and implants do not transfer the load properly. Wolff's law states that bones change according to the mechanical load they get, which means that more bone is formed to make the tissue stronger when a person does more activity in a certain area of the body. On the other hand, when a bone does not bear any load for a long time, the tissue mass can reduce with bone

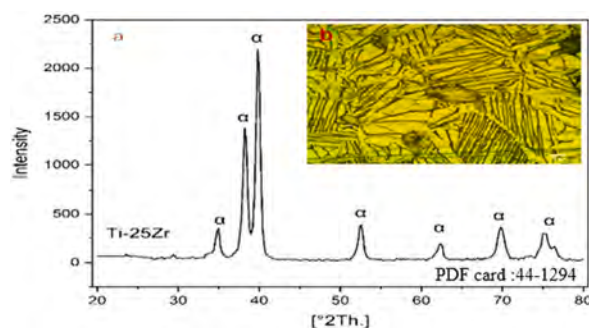


Fig. 1. (a)XRD patterns of Ti–25Zr alloys,(b)Optical micrograph shows α phase microstructure of Ti–25Zr alloy surface at $800\times$.

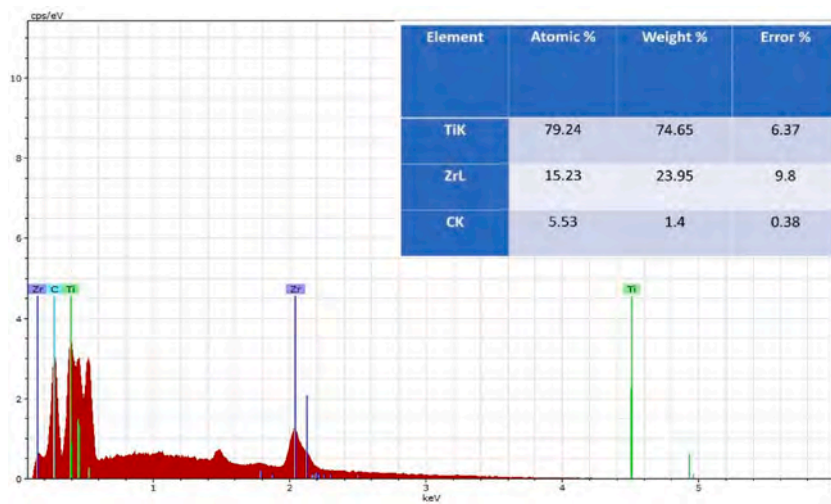


Fig. 2. EDS analysis of the surface of Ti–25Zr alloy.

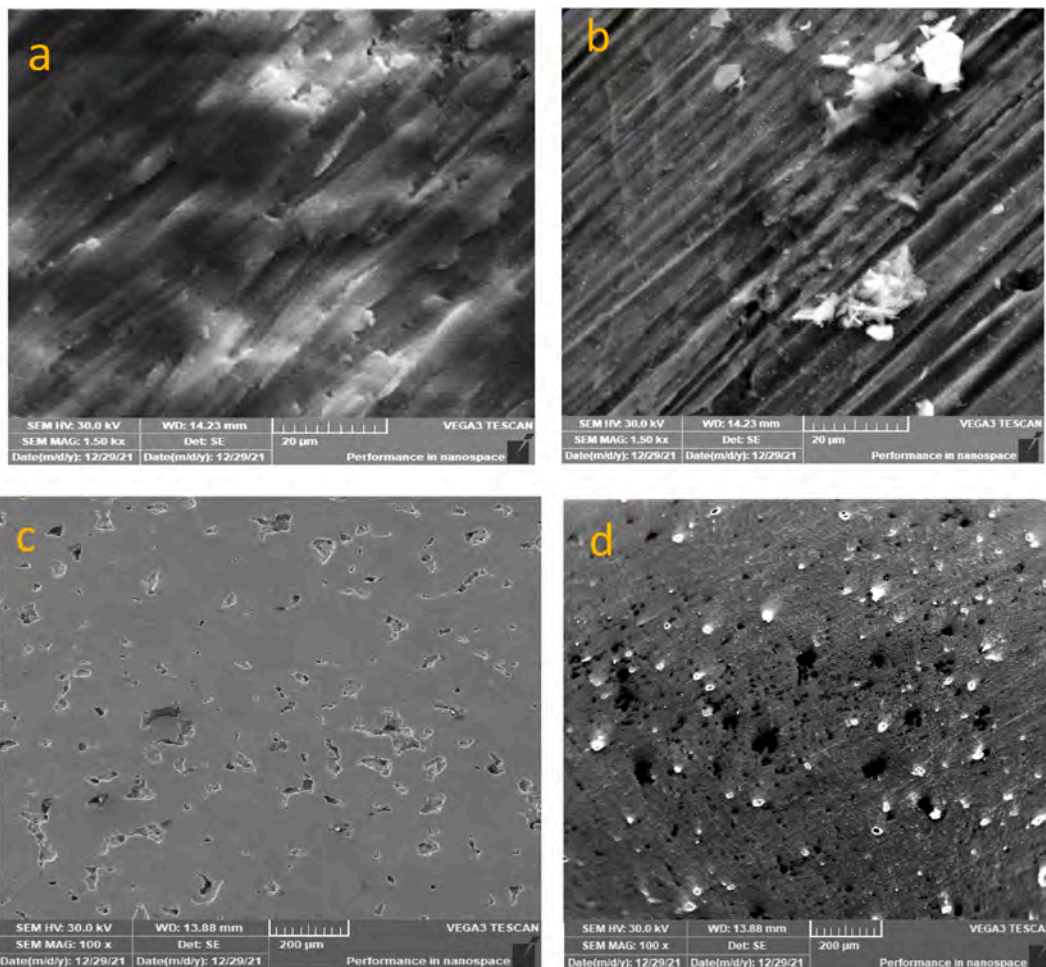


Fig. 3. SEM images show the texture of the surface before and after acid and alkaline treatment. Images (a) and (c) show the surface before treatment, while images (b) and (d) show the surface after treatment. The treatment caused the surface to become more rough and textured.

Table 1
Ti–25Zr alloy mechanical and physical characteristics.

Microhardness, Hv	283 ± 21
Compression strength, MPa	713 ± 79.3
Tension strength, MPa	453 ± 33.4
Elastic Modulus, GPa	78 ± 8.1
Apparent density	4.46 ± 0.02
Porosity %	9 ± 0.36

resorption [30]. If the implant has a higher elastic modulus, it may not effectively transfer loads to the surrounding bone undergoing remodeling. This can cause a phenomenon known as stress shielding, which could result in bone loss and potential implant failure [31, 32]. The Ti–Zr alloy has garnered considerable attention in research due to its reduced modulus of elasticity and improved mechanical and biological characteristics. In contemporary times, there has been substantial progress in the evolution of porous titanium alloys. These titanium alloys are engineered with porous structures that effectively decrease the elastic modulus of the implant's to levels similar to natural bone. This enables the growth of new bone within the porous region and facilitates mechanical interlocking [21,26, 33].

3.4. Characterization of electrospun fiber

The topology of the nanocomposite fiber was detected using field-emission scanning electron microscopy (FESEM). The fibers' average diameter and pores were assessed using Image J, a software tool provided by the (US National Institutes of Health, Bethesda, Maryland, USA). Additionally, an energy dispersive X-ray spectrometer (EDS) was utilized to identify the presence of chemical elements. Composite nanofiber (BA1, SR1), homogeneously distributed bead-free non-woven fibers are visible. (Figs. 4–5 a). The diameter of fiber (BA1) ranges from (94.112) to (280.399 nm) having an average diameter of (178.58 ± 47.023 nm) and an average pore size of (1176.742 ± 517.69 nm) (Fig. 4 c and d). EDS analysis (Fig. 4 b) shows that fiber-containing (Ba) which was related to utilizing (BaTiO₃) (Fig. 5 c-d). Displays that the diameter of (SR1) fibers range (111.23–321.197 nm) having diameter of an average

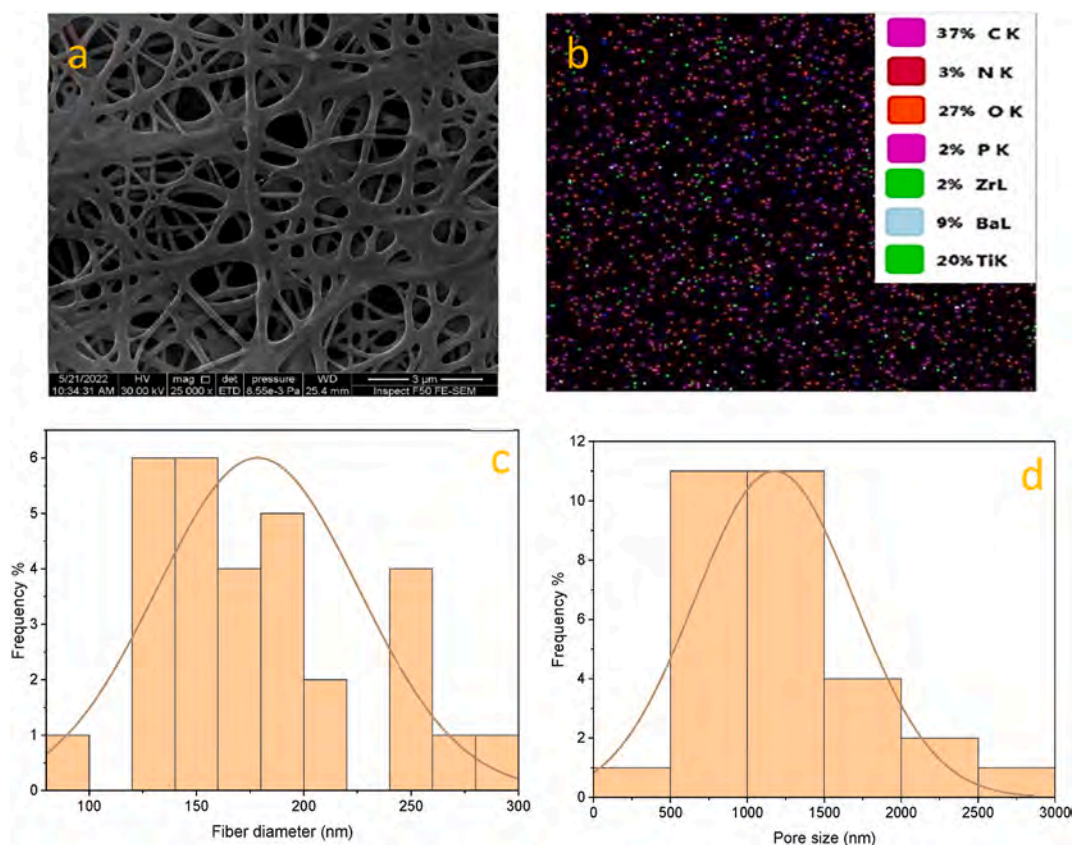


Fig. 4. (a) FESEM, (b) EDS, (c) distribution of fiber diameters, (d) distribution of pore sizes. Concerning PCL/CS/Nano-BaTiO₃ (BA1) Nano-composite fiber.

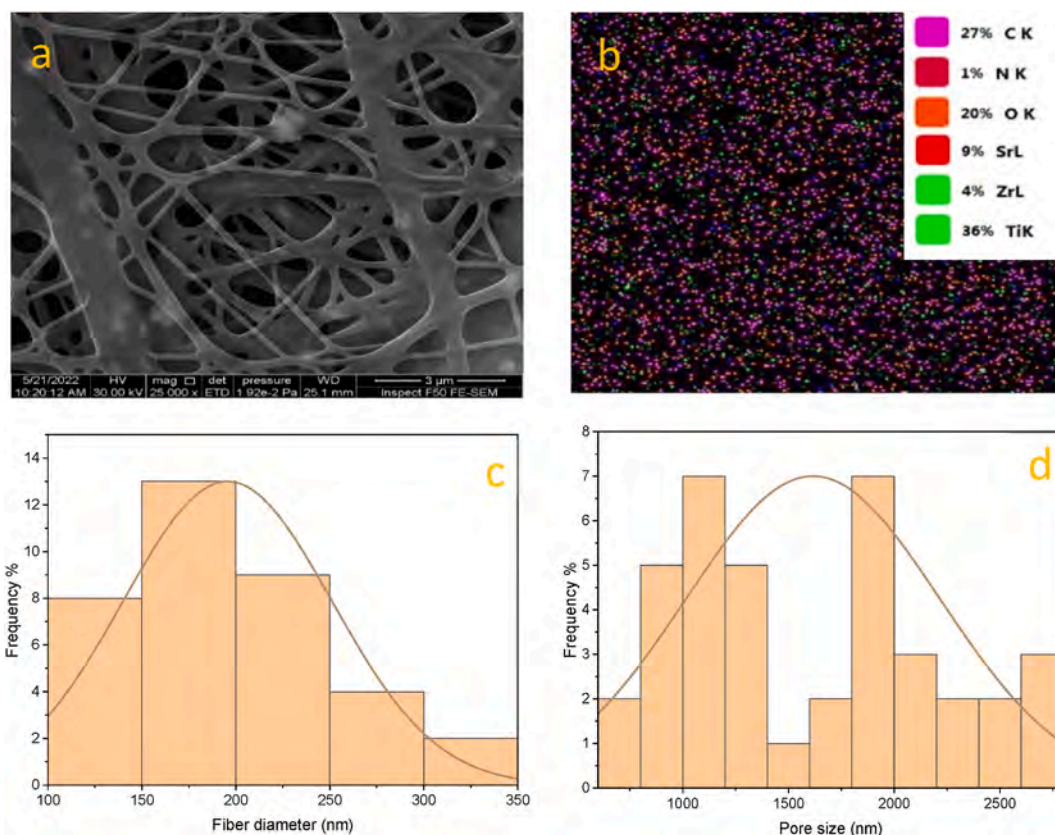


Fig. 5. (a) FESEM, (b) EDS, (c) distribution of fiber diameters, (d) distribution of pore sizes. Concerning PCL/CS/Nano-SrTiO₃ (SR1) Nano-composite fiber.

(195.54 ± 9.25 nm) and the pore size average of (1615.99 ± 96.11 nm) and EDS prove the existence of strontium in relation to the incorporation of SrTiO₃ into the precursor (Fig. 5 b).

The cross-sectional structure of the coated specimens was examined using FESEM (Fig. 6 a,c). shows the image of the cross-section for BA1/Ti-25Zr and SR1/Ti-25Zr layers respectively. It can be seen that both BA1 and SR1 have a dense, uniform, and even layer over metal substrates. The film thickness of the two coatings is comparable, BA1 has 155.8 μm, and SR1 has 160.3 μm thickness. The thickness can be adjusted by controlling the time of coat applied. There are no cracks or defects on both coating layers and no delamination in the interface between the coating layer and the metal surface, suggesting that the adhesive strength between them is good. The substrate's chemical composition (EDX) was shown in Fig. 2; only Ti and Zr elements were found, while (EDX) of the upper coating layer revealed more elements to be involved in the composition of the coating layer (Fig. 6 b,d).

3.5. Microhardness and adhesion of coating layers

The average value of microhardness for nanofiber-coating layers over Ti-25Zr substrate was measured. BA1 (PCL/chitosan/BaTiO₃) has a value of 24.44HV, while SR1 has 20.78HV, revealing that BA1 has more strength than SR1. The same trend was observed when evaluating the adhesion of coating layers by scratch test, where BA1 adhesion strength is better than that of SR1 (Fig. 7) shows a qualitative image of the scratch test used to compare the scratch result between different coats. The optical image (Fig. 7 a,c) at load 1 N for both coating layers did not fail, and the layer resisted load. As the load continues to rise, the width and depth of the scratch increase to reach the metal surface at a load of 1.8 N for BA1 and 1.5 N for SR1 (Fig. 7 b,d). The result shows that the coating layer containing BaTiO₃ has more strength than SrTiO₃, which may be attributed to the different elastic properties of BaTiO₃ and SrTiO₃, as BaTiO₃ has a higher elastic modulus than SrTiO₃. Elastic modulus of BaTiO₃ is 190 GPa, while that of SrTiO₃ is 130 GPa [34].

3.6. Dielectric behavior and polarizability

The dielectrics are electrically insulating materials that can generate dipoles without or with an external electric field by the relative motion or separation of positive and negative charges. The term for this is polarization. The dielectric constant quantifies the polarizability of a dielectric substance in response to an external stimulus [35].

The polarizability of living, natural bone results from the hydrogen bond between collagen and hydroxyapatite. The dielectric

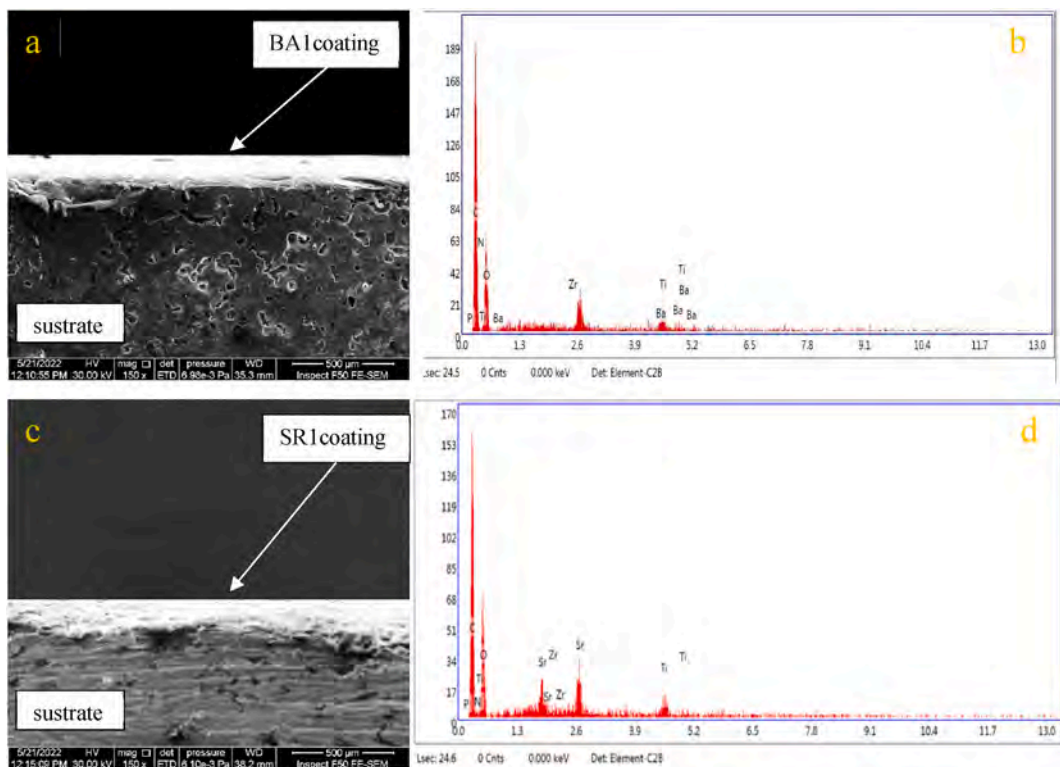


Fig. 6. The SEM micrograph and EDX analysis were conducted on the cross-section of the BA1 coating layer, represented by (a,b), and the SR1 coating layer, represented by (c,d).

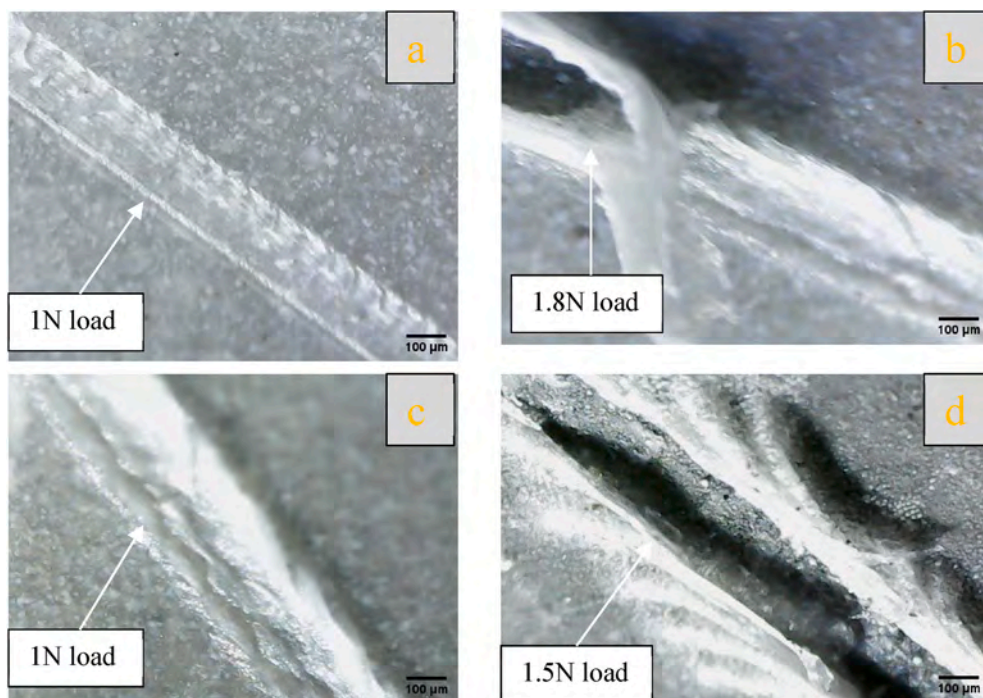


Fig. 7. Optical microscopy captured images of the coating following a scratch test, depicting (a,b) for BA1 and (c,d) for SR1.

characteristics of bone change based on frequency and moisture content. Studies have indicated that the dielectric constant of dry human bone is around 10 over the frequency range of 1–100 kHz [35–37].

After measuring the electrical capacity of each composite sample, the dielectric constant was determined through equation (5), as shown in (Fig. 8). The findings suggest the category of nano-ceramic compound affects the electrical properties of PCL/CS/nano-ceramic composites. It is revealed that the Nano-BaTiO₃ content improved the dielectric constant. Furthermore, various polarization mechanisms still have an influence through lower frequency ranges, including electronic, ionic, and oriental polarization. However, at higher frequencies, the value of ϵ_r experiences a change due to the incapacity of dipoles present in thin films to adapt to the frequency alteration of the field that applied., resulting in a diminution in thin film polarization [38].

In addition, a significant decrease in dielectric constant was observed at high frequency in composites containing Sr²⁺. This is due to the existence of strontium in the formulation. A reduction in the network constant due to Sr²⁺ limits the oscillation range of titanium ions (Ti²⁺) and alters the structure of the ferroelectric domain. The effects on a dielectric constant, such as increasing or decreasing based on the amount of available (Sr) [39].

From a biomedical standpoint, the ϵ_r of coated implants can be used to determine the fracture recovery rate. It is now standard practice in medicine to use external electric fields to accelerate fracture healing. The mechanism underlying the process of healing is unknown; however, its effects are incredibly beneficial. When complicated cases involve the using of implants with an electroactive coating that can undergo polarization might aid in enhancing the healing process. Moreover, more significant cell proliferation is associated with a higher value of ϵ_r , which in turn is related to polarization and plays a vital role in diverse biological applications, ultimately leading to an accelerated healing process [38].

3.7. Fourier-transform infrared spectroscopy (FT-IR)

The FTIR absorption spectra of PCL, CS, ceramic nano-additives (nBaTiO₃ and nSrTiO₃), and the electrospun fiber composite coating of PCL/CS/nBaTiO₃ and PCL/CS/nSrTiO₃ are shown in (Figs. 9 and 10). The carbonyl group of the ester group is responsible for the dominant peak at 1723 cm⁻¹ in pure PCL spectra. Moreover, an asymmetric CH₂ stretching peak was seen at 2943 cm⁻¹, while a symmetric CH₂ stretching peak was observed at 2869 cm⁻¹. The symmetric and asymmetric C–O–C stretching modes corresponded to the bands at 1239, 1161, 1107, and 1045 cm⁻¹, respectively, while the C–O and C–C stretching modes were related to the absorption peak at 1294 cm⁻¹ [13,40].

The carboxylate ion of chitosan exhibited a prominent peak at 1726 cm⁻¹, while the chitosan spectra displayed a wide band around 3245 cm⁻¹, which may be due to the stretching vibrations of O–H and N–H. Additionally, peaks at 2945 and 2897 cm⁻¹, corresponding to the symmetrical and asymmetrical methylene groups, respectively, were observed. Furthermore, a spectrum ranging from 1180 to 1063 cm⁻¹, indicative of the saccharide structure of chitosan, was also detected. The central frequency of the chitosan band relevant to the stretching of the C=O bond in amide I was found to be 1615 cm⁻¹, which is rather noteworthy. Similarly, the observed peak at a wavenumber of 1510 cm⁻¹ may be associate with amide II band. Furthermore, the observed sample exhibited a discernible spectral feature attributed to the C–C aromatic stretching vibration, which manifested as a discrete band at a wavenumber of 1420 cm⁻¹. There are three distinct peaks seen within the wavenumber range of 1020–1140 cm⁻¹, which may be relevant to the symmetric and asymmetric modes of C–O–C stretching [40–42].

For the titanite nano-compound (BaTiO₃) (Fig. 9), showed peaks of vibration that had clear signs of a stretching band in the region (410–559 cm⁻¹) that were related to the (Ti–O) [13]. There was also a Ba–Ti–O band found at 597 cm⁻¹ [43]. The existence of the hydroxyl group is revealed by the peak at 1647 cm⁻¹ associated with the content of molecular water of (O–H) band vibration, in contrast to the weak hydroxylate (O–H) band that is also existing in 3378 cm⁻¹ for BaTiO₃ [44,45]. BaTiO₃–OH is responsible for the

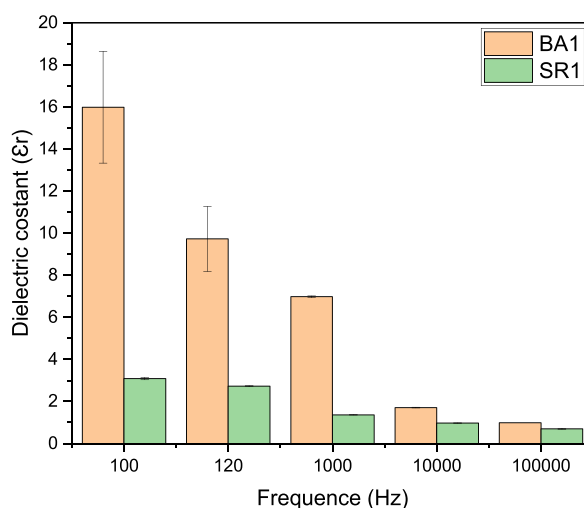


Fig. 8. Dielectric constant calculation at a range of frequencies for composite coating.

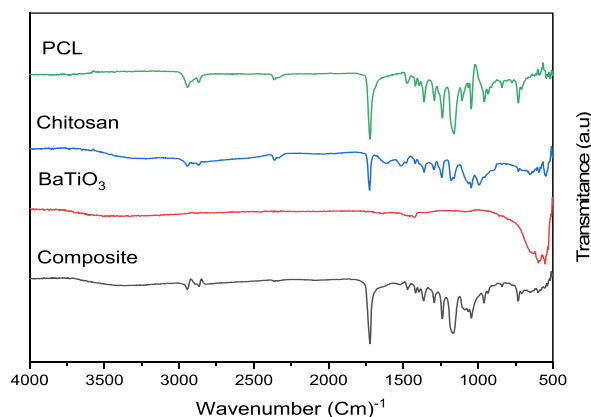


Fig. 9. FT-IR comparison of pure (PCL, CS, nBaTiO₃) and synthesized (8% w/v PCL, 2% w/v CS, 1% w/v nBaTiO₃).

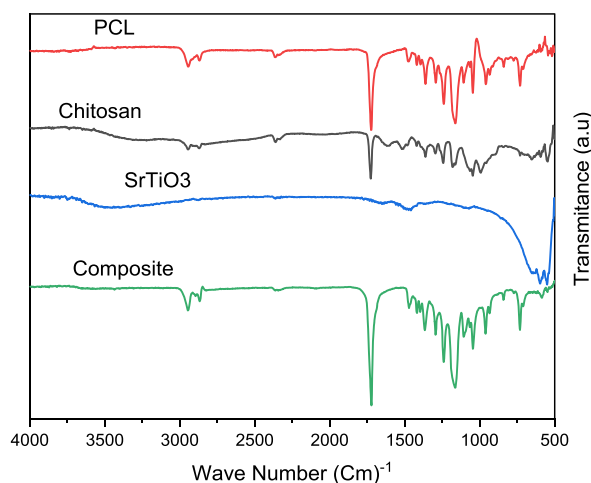


Fig. 10. FT-IR comparison of pure (PCL, CS, nSrTiO₃) and synthesized (8% w/v PCL, 2% w/v CS, 1% w/v nSrTiO₃).



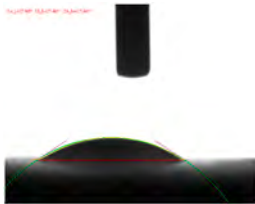
peak that is observed at 1430 cm^{-1} for BaTiO₃ [46].

In order to examine the incorporation of SrTiO₃ NPs, absorption analysis using FTIR spectroscopy can be utilized (Fig. 10). The spectra still exhibit the stretching and bending vibrations of the TiO₆ octahedron, along with prominent absorption bands centered around 425 and 650 cm^{-1} . The absorption at 3300 cm^{-1} is attributed to the stretching vibration of the surface hydroxyl group, while the remaining minor peak at approximately 1630 cm^{-1} is associated with the bending vibration of physically adsorbed water (H–O–H) [47].

The Fourier-transform infrared (FTIR) analysis of both composite coatings (PCL/CS/nBaTiO₃ and PCL/CS/nSrTiO₃) verified the composite layer that is formed is novel and uniform. This confirmation was obtained through the detection of a stretching vibration

Table 2

Measurements of the contact angle for various composite coating types.

Sample	Control Bare (Ti–25Zr)	BA1 (PCL/Chitosan/nBaTiO ₃)	SR1 (PCL/Chitosan/nSrTiO ₃)
Contact angle	$43.642^\circ \pm 8.8$	$18.534^\circ \pm 5.4$	$27.468^\circ \pm 7.4$
			

peak within a similar range to its individual components, albeit with a slight shift towards lower wavenumbers.

3.8. Contact angle and wettability

One of the main points of contact between a metallic implant and the living tissue is the implant's surface. The metal surface hydrophilicity may significantly influence the serum proteins adsorption as well as the osteoblasts and bacteria adhesion behavior. The coating and the uncoating samples contact angles as shown in (Table 2), ranged from 43.642° to 18.534°, suggesting that all sample surfaces were hydrophilic.

Ti-25Zr, the reference sample, exhibits poor wettability. Acid and base treatment increased the roughness of the surface and its energy, which caused the contact angle to reduce significantly values, which became hydrophilic at a contact angle of 43.642° after being hydrophobic. This is a positive thing for biocompatibility and cell adhesion [23,48].

The findings also show that the wettability of the sample with a composite-coated surface has improved. Due to the high porosity and roughness of the surfaces, the existence of amino groups, and the hydroxyl group of chitosan, which is bonded to the hydrogen in water molecules as a consequence, the coatings were hydrophilic [49].

The composite coating containing Nano (BaTiO₃, SrTiO₃) ceramic compounds incorporated with polymers has a low angle of 18.534° and 27.468°, respectively, as shown in (Table 2), that may be associated with the existence of nanoceramics filler particles that increase hydrophilicity and, in conjunction with chitosan, improve wettability [3,50].

3.9. Bacterial resistance evaluation

In the fields of orthopedics and dentistry, where implants are used, developing biomaterials that are resistant to the growth of microbes is a serious challenge. Chitosan is frequently employed as a bactericidal agent, either by itself or in conjunction with other natural polymers, due to its nontoxicity, antibacterial, and high biodegradability properties [51,52]. The inclusion of the filler nano-ceramic (BaTiO₃, SrTiO₃) with chitosan was also described as a bacterial resistance substance, enhancing the total inhibitory zone surrounding the coating (Fig. 11(a–f)).

The antibacterial test employed bacterial spaciuous, namely *Streptococcus mutans* (*S. mutans*) and *Staphylococcus aureus* (*S. aureus*). All the composite coating (PCL/CS/nBaTiO₃, PCL/CS/nSrTiO₃) Demonstrate similar and effective antibacterial outcomes for both types of bacteria, which are illustrated in Fig. 12.

Nano-BaTiO₃ has been found to exhibit antibacterial properties, which may be explained by the blocking ergosterol production results in cell mortality [53]. Furthermore, a new approach for electrically polarizing biocompatible ceramics with or without piezoelectric properties, such as BaTiO₃, has been proposed to create antimicrobial implants. The survival of *Staphylococcus aureus* (*S. aureus*) and *Escherichia coli* (*E. coli*) on charged surfaces was markedly decreased. Polarization's effect on antibacterial response has been investigated through multiple processes, encompassing the production of reactive oxygen species, lipid oxidation, and the function of the catalase enzyme [54].

As reported, sustained release of Sr²⁺ from STF powder near the attached *E. coli* can induce membrane malfunctions, resulting in cell demise. According various tests, including surface charge assessment, fluorescence microscopy inspection, inductively coupled plasma metrics, and scanning electron microscopy (SEM) examination, suggest that the remarkable bactericidal capability of the STF_{0.8} metal oxide can be credited to its positive surface charge, elevated pH surroundings, Sr²⁺ dissociation, and its nanoscale particles [55].

3.10. In vitro cytocompatibility assay

3.10.1. Cell activity and morphology

The way the implant and the host tissue interact with each other depends on the cell attachment, survival, and growth at the interface. This is an important factor during the implantation process. Because of its biocompatibility and ability to promote cell growth, the application of titanium and its alloys in medicine is increasing. Surface activation is necessary for these biometallic alloys

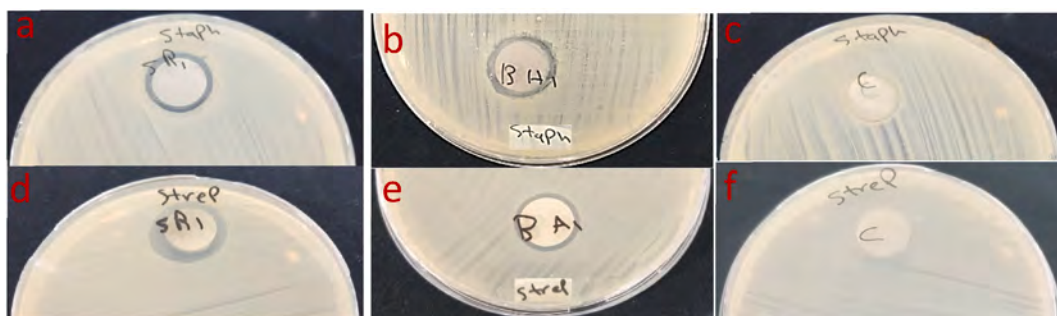


Fig. 11. (a–c) the inhibition zones for *Staphylococcus aureus* (*S. aureus*), and (d–f) the inhibition zones for *Streptococcus mutans* (*S. mutans*).

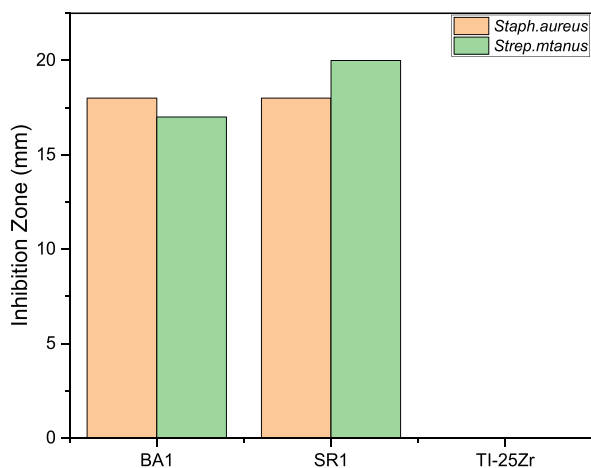
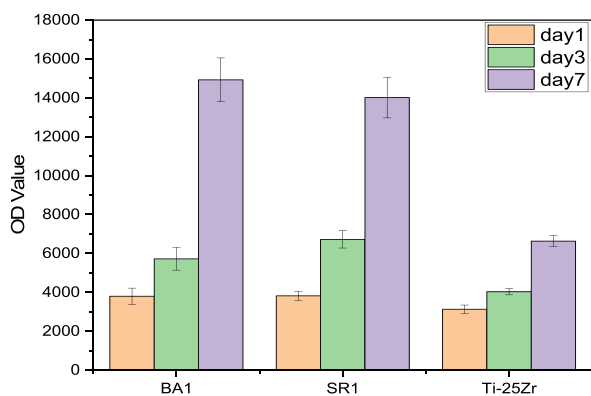
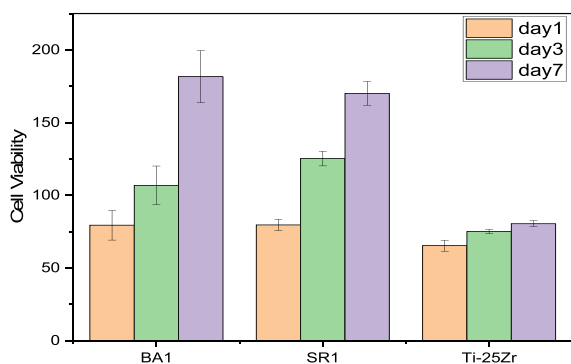


Fig. 12. Measurement of the inhibition zone of the non-coated and coated samples.



a



b

Fig. 13. (a) MC3T3-E1 cell proliferation activity was detected by Alamarblue. Regarding proliferation rate, both BA1 and SR1 showed a significant difference when compared to Ti-25Zr ($p < 0.0001$ for BA1, $p = 0.00014$ for SR1), while there was no noticeable difference between BA1 and SR1 ($p = 0.4743$). (b) The percentage of live cells in relation to the total number of cells was used to express the cell viability. The same trend was observed in the case of cell viability with a statistically significant difference between BA1 and Ti-25Zr ($p < 0.0001$, for BA1 vs. Ti-25Zr), followed by SR1, ($p = 0.000176$, for SR1 vs. Ti-25Zr). Although there is no significant difference between BA1 and SR1 ($p < 0.47506$, for BA1 vs. SR1).

to facilitate cell interaction and prevent bacterial infection due to the inert surface and the risk of bacterial contamination (Fig. 13a and b). show the results of an investigation of the cytocompatibility of uncoated and coated Ti–25Zr alloys utilizing cell line MC3T3-E1 and the Alamarblue assay.

The cell proliferation of uncoated and coated Ti–25Zr alloys cultivated with MC3T3-E1 cells for 1, 3, and 7 days are depicted in (Fig. 13a). Indicating that cell proliferation takes place on both coated and uncoated samples, the cell proliferation values for the uncoated and coated Ti–25Zr alloy display a remarkable rise with increasing culture times. Yet, at every given time interval, the cell proliferation rates of the coated sample consistently surpassed those of the uncoated one, reaching a maximum on day seven. The (BA1) coated sample exhibited the maximum rate of cellular proliferation, with a 125.16% increase compared to the non-coated sample, followed by (SR1) with a rise of 111.38%.

Compared to the uncoated sample, the cell viabilities of the BA1 and SR1 samples are higher at all intervals (Fig. 13 b). The coated sample has a much higher cell viability than the non-coated sample, which has $80.52 \pm 1.97\%$, so (BA1) has $181.63 \pm 17.87\%$ and (SR1) has $170.09 \pm 8.12\%$. On day 7, coated samples exhibited a much higher level of cell viability than uncoated samples. ($p < 0.0001$, for BA1 vs. Ti–25Zr; $p < 0.000176$, for SR1 vs. Ti–25Zr). (BA1) coated have no significant cell viability than (SR1) ($p < 0.47506$, for BA1 vs. SR1). According to the cell toxicity classification standard, with a cell viability of more than 75%, the non-coated porous Ti–25Zr alloy is a Grade 1 material that is not cytotoxic. With a cell viability exceeding 100%, the coated surface Ti–25Zr alloy is a non-cytotoxic Grade 0 material for biomedical applications [56,57]. When the optical density (OD) values and cell activities are combined, it is possible to conclude that coated and non-coated samples have no cytotoxicity and great cytocompatibility with MC3T3-E1 cells. The electrospinning coating with composite fiber can significantly increase Ti–25Zr alloy bioactivity and cytocompatibility.

ALP is a marker of the first stage of osteogenic differentiation and is crucial for the regeneration of bone mineralization (Fig. 14). depicts a quantitative examination of ALP activity. The ALP activity in all samples increased over time. After three days, the ALP activity of the non-coated and coated samples is not significantly different. This may be caused by the time that the coating layer spends to become mineralized and interact with the body's host media. On day 7, cells on coated samples had significantly higher ALP activity than cells on non-coated samples ($p = 0.0105$, for BA1 vs. Ti–25Zr; $p = 0.02225$, for SR1 vs. Ti–25Zr). (BA1) coated sample presented a nonsignificant value when compared to (SR1), ($p = 0.78216$, for BA1 vs. SR1).

The MC3T3-E1 cells' osteogenic differentiation was increased by incorporating BaTiO₃ nanoparticles into PCL/Chitosan blended polymer. The osteoblast-like cells' proliferation, vitality, and extracellular matrix deposition were significantly enhanced by the piezoelectric action of BaTiO₃ created in the nanocomposite fiber produced via electrospinning. This finding is consistent with previously reported results, demonstrating that the piezoelectric performance of piezoelectric polymer composites is significantly affected by the viscosity and elasticity of the polymer. When combined with barium titanate, chitosan, which has a deacetylation degree of 91.2%, demonstrates piezoelectric characteristics and enhances cell activity [10,13].

Previous research has shown that the coating layer, which includes strontium titanate (SrTiO₃) nano-particles promotes cell proliferation. Sr²⁺ ions increased cell survival and proliferation, which could be explained by the activation of the CaSR, a receptor that senses calcium, and the capability of Sr ions to boost the pre-osteoblastic cells to differentiate while inhibiting osteoclasts [16,58,59].

(Fig. 15(a–f)) SEM image illustrates the culture of the cells MC3T3-E1 on both coated and uncoated samples after a period of 7 days. It was found that the MC3T3-E1 cells was deposited randomly on a forward Ti–25Zr alloy surface and aligned with a somewhat circular shape (Fig. 15(e and f)). In contrast, the surface of the coated sample caused the formation of preferable sites for the deposition cells with typical osteoplastic polygonal morphology over 7 days. The MC3T3-E1 cell becomes anchored to the composite mat-like coated layer pattern with micro and nanostructure that become a platform for further spreading the cell inducing cell growth and metabolism (Fig. 15a–d). MC3T3-E1, after 7 days of culture on the coated surface, indicate the beginning of lamellipodia formation. The cell process is extended on the rougher surface, so the three-dimensional shape cell is developed more consistently with physiological

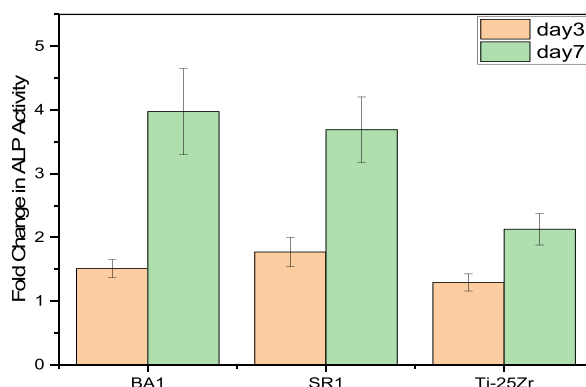


Fig. 14. Fold change of ALP activity in MC3T3-E1 cells on samples with and without coating at 3 and 7 days of culture. On day 7, cells on BA1-coated samples had significantly higher ALP activity than uncoated Ti25Zr ($p = 0.0105$, for BA1 vs. Ti–25Zr). SR1-coated samples also had a significant advantage over uncoated Ti25Zr ($p = 0.02225$, for SR1 vs. Ti–25Zr). While the (BA1) coated samples did not differ significantly from (SR1), ($p = 0.78216$, for BA1 vs. SR1).

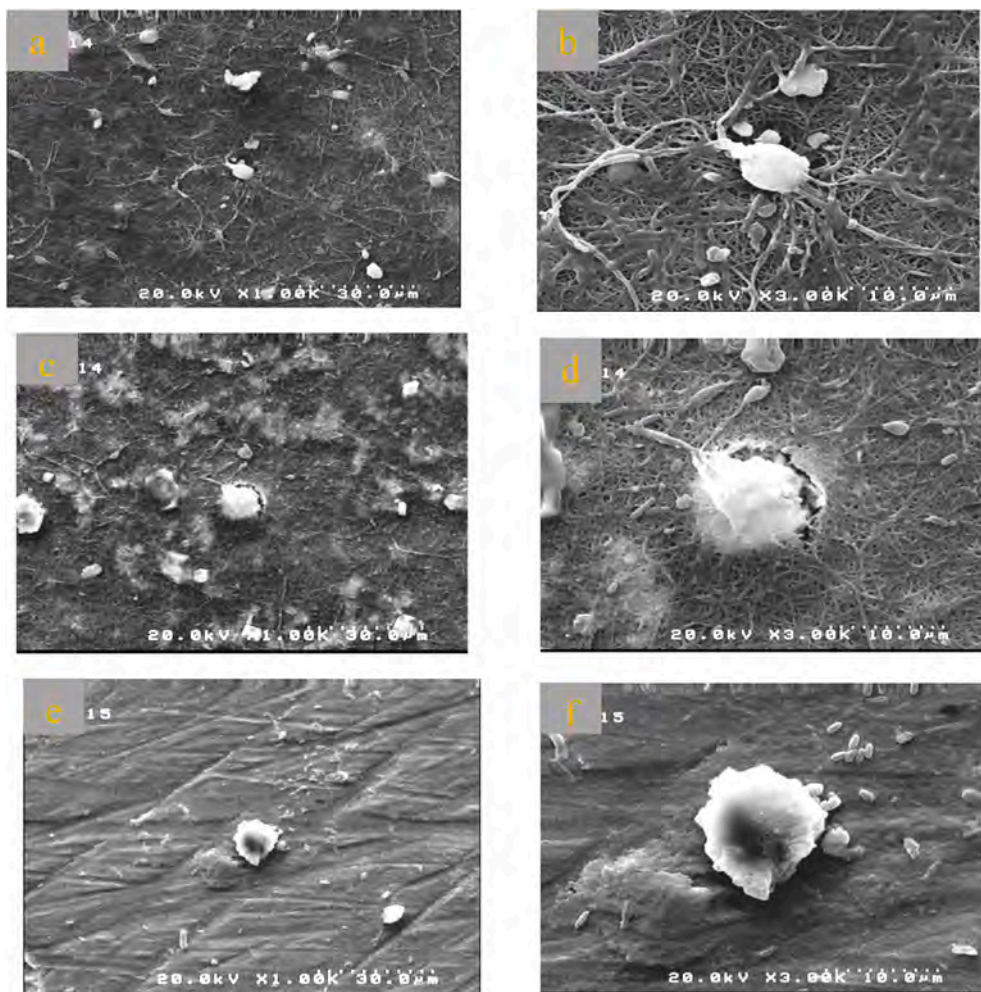


Fig. 15. Images taken by scanning electron microscopy (SEM) of cultured MC3T3-E1 cells for 7 days on the surface of (a-b)BA1, (c-d)SR1, (e-f) bare Ti-25Zr.

attachment. One of the reasons for the increased cell attachment capacity on the coated surface is its low-contact angle, which promotes greater protein absorption from culture media. It was found that all of the coating surfaces produced using electrospinning resulted in higher cell proliferation compared to the uncoated sample.

3.11. Conclusion

In this work, active nano-ceramic compounds such as piezoelectric BaTiO_3 and perovskite SrTiO_3 were dipped individually in a blended polymer of PCL/Chitosan to create two solutions ready for use in an electrospinning coat to apply on the Ti-25Zr alloy surface as composite nano-fiber to promote cell viability and resist bacterial infections. The coated surface characterization was examined, its biocompatibility was evaluated, and it was concluded the following.

- 1 Ti-Zr alloy prepared by powder metallurgy form completed solid solution with superior mechanical properties compared to cp-Ti, except for the modulus of elasticity, which is reduced by 29%, and this benefit for bioimplant in reduced stress shielding.
- 2 The coating process through electrospinning produces nano-fibers with a nano-rough surface, high contact area, and porosity, which promotes a favorable reaction with the physiological medium. This enhances the ability of cells to adhere and proliferate.
- 3 The composite coating containing piezoelectric BaTiO_3 has a dielectric constant close to dry human bone.
- 4 The coated samples show a hydrophilic surface with low contact angle
- 5 The samples with coating have a reasonable and comparable zone of inhibition, which means they can resist bacterial growth. The sample without coating does not have any zone of inhibition, which means it is susceptible to bacterial infection.
- 6 Compared to non-coated samples, the coated samples significantly improved cell viability, proliferation, and differentiation.

Author contribution statement

Amjed Al-Khateeb: Performed the experiments; Contributed reagents, materials, analysis tools, or data; Wrote the paper.
Emad S. Al-Hassani & Akram R. Jabur: Conceived and designed the experiments; Analyzed and interpreted the data.

Data availability statement

Data will be made available on request.

Additional information

No additional information is available for this paper.

Declaration of competing interest

The authors declare that they have no known competing financial interests or personal relationships that could have appeared to influence the work reported in this paper.

References

- [1] M.J. Dewey, B.A.C. Harley, Biomaterial design strategies to address obstacles in craniomaxillofacial bone repair, *RSC Adv.* 11 (2021) 17809–17827, <https://doi.org/10.1039/d1ra02557k>.
- [2] É.L. Rosero-Alzate, M.Á. Zapata-Pernett, D. Vega-Ortiz, L.D. Puerta-Tinoco, M.C. Múnera-Ramírez, J. Esguerra-Arce, A. Esguerra-Arce, Influence of porosity on the biomimetic growing patterns of bone-like apatite on the surface of calcium phosphate – calcium titanate – alumina compounds, *Dyna* 88 (2021) 24–33, <https://doi.org/10.15446/dyna.v88n218.91651>.
- [3] G.N. Schädli, H. David, A.M. de Leeuw, F. Carlson, L. Tenisch, P. Muff, M. Rubert, R. Müller, Optimizing barium titanate nanocomposite bone scaffolds for biomineralization in dynamic compression bioreactors using time-lapsed microstructural imaging and smart thresholding, *Front. Mater.* 8 (2022) 1–15, <https://doi.org/10.3389/fmats.2021.796044>.
- [4] K. Pajor, A. Michalicha, A. Belcarz, L. Pajchel, A. Zgadzaj, F. Wojas, J. Kolmas, Antibacterial and cytotoxicity evaluation of new hydroxyapatite-based granules containing silver or gallium ions with potential use as bone substitutes, *Int. J. Mol. Sci.* 23 (2022), <https://doi.org/10.3390/ijms23137102>.
- [5] E. Al-Hassani, F. Al-Hassani, M. Najim, Effect of polymer coating on the osseointegration of CP-Ti dental implant, *AIP Conf. Proc.* (2018), <https://doi.org/10.1063/1.5039209>, 1968.
- [6] D.E.S. Al-Hassani, Effect of (Ta & Nb) on corrosion behavior of nitinol alloys, *Eng. & Tech. Journal.* 34 (2016) 1894–1902.
- [7] A. Rodríguez-Contreras, D. Torres, B. Rafik, M. Ortiz-Hernandez, M.P. Ginebra, J.A. Calero, J.M. Manero, E. Ruperez, Bioactivity and antibacterial properties of calcium- and silver-doped coatings on 3D printed titanium scaffolds, *Surf. Coating Technol.* 421 (2021), <https://doi.org/10.1016/j.surfcoat.2021.127476>.
- [8] T. Lai, J.L. Xu, X. Cao, L.Z. Bao, J.M. Luo, Y.Z. Huang, Bioactive CaTiO₃ film prepared on the biomedical porous Ti–15Mo alloy by one-step hydrothermal treatment, *J. Mater. Res. Technol.* 14 (2021) 202–209, <https://doi.org/10.1016/j.jmrt.2021.06.065>.
- [9] R. Rawdan, M. Abdulkareem, A. Mustafa, Optimizing of coating layers parameters of (nano hydroxyapatite/TiO₂ NPs) on nitinol SMAs by electrophoretic deposition, *Eng. Technol. J.* 38 (2020) 530–544, <https://doi.org/10.30684/etj.v38i4a.577>.
- [10] E. Prokhorov, G.L. Bárcenas, B.L. España Sánchez, B. Franco, F. Padilla-Vaca, M.A. Hernández Landaverde, J.M. Yáñez Limón, R.A. López, Chitosan-BaTiO₃ nanostructured piezopolymer for tissue engineering, *Colloids Surf., B* 196 (2020), 111296, <https://doi.org/10.1016/j.colsurfb.2020.111296>.
- [11] A. Das, P. Dobbidi, A. Bhardwaj, V. Saxena, L.M. Pandey, Microstructural, electrical and biological activity in Ca₁₀(PO₄)₆(OH)₂-Ba_{0.5}Sr_{0.5}TiO₃ ceramic composites designed for tissue engineering applications, *Sci. Rep.* 11 (2021) 1–15, <https://doi.org/10.1038/s41598-021-01748-8>.
- [12] M. Fakhar-e-Alam, S. Saddique, N. Hossain, A. Shahzad, I. Ullah, A. Sohail, M.J.I. Khan, M. Saadullah, Synthesis, characterization, and application of BaTiO₃ nanoparticles for anti-cancer activity, *J. Cluster Sci.* (2022), <https://doi.org/10.1007/s10876-022-02346-y>.
- [13] E. Mancuso, L. Shah, S. Jindal, C. Serenelli, Z.M. Tsikriteas, H. Khanbareh, A. Tirella, Additively manufactured BaTiO₃ composite scaffolds: a novel strategy for load bearing bone tissue engineering applications, *Mater. Sci. Eng., C* 126 (2021), 112192, <https://doi.org/10.1016/j.msec.2021.112192>.
- [14] J.P. Ball, B.A. Mound, J.C. Nino, J.B. Allen, Biocompatible evaluation of barium titanate foamed ceramic structures for orthopedic applications, *J. Biomed. Mater. Res., Part A* 102 (2014) 2089–2095, <https://doi.org/10.1002/jbm.a.34879>.
- [15] A. Das, A. Bhardwaj, S. Rabha, L.M. Pandey, P. Dobbidi, Physical, chemical, and biological investigations of SrTiO₃-Ca₁₀(PO₄)₆(OH)₂ composites for biomedical applications, *J. Am. Ceram. Soc.* 105 (2022) 1790–1808, <https://doi.org/10.1111/jace.17952>.
- [16] A. Escobar, N. Muzzio, P.C. Angelomé, A.V. Bordini, A. Martínez, E. Bindini, E. Coy, P. Andreozzi, M. Grzelczak, S.E. Moya, Strontium titanate (SrTiO₃) mesoporous coatings for enhanced strontium delivery and osseointegration on bone implants, *Adv. Eng. Mater.* 21 (2019) 1–8, <https://doi.org/10.1002/adem.201801210>.
- [17] A.R. Jabur, E.S. Al-Hassani, A.M. Al-Shammari, M.A. Najim, A.A. Hassan, A.A. Ahmed, Evaluation of stem cells' growth on electrospun polycaprolactone (PCL) scaffolds used for soft tissue applications, *Energy Proc.* 119 (2017) 61–71, <https://doi.org/10.1016/j.egypro.2017.07.048>.
- [18] A.R. Jabur, Antibacterial activity and heavy metal removal efficiency of electrospun medium molecular weight chitosan/nylon-6 nanofibre membranes, *Biomed. Mater.* 13 (2018), <https://doi.org/10.1088/1748-605X/aa9256>.
- [19] Y. Wu, G. Sriram, A.S. Fawzy, J.Y.H. Fuh, V. Rosa, T. Cao, Y.S. Wong, Fabrication and evaluation of electrohydrodynamic jet 3D printed polycaprolactone/chitosan cell carriers using human embryonic stem cell-derived fibroblasts, *J. Biomater. Appl.* 31 (2016) 181–192, <https://doi.org/10.1177/0885328216652537>.
- [20] O. Differentiation, R.J. Kroeze, M. Knippenberg, M.N. Helder, in: J.M. Gimble, B.A. Bunnell (Eds.), *Osteogenic Differentiation Strategies for Adipose-Derived Mesenchymal Stem Cells BT - Adipose-Derived Stem Cells: Methods and Protocols*, Humana Press, Totowa, NJ, 2011, pp. 233–248, https://doi.org/10.1007/978-1-61737-960-4_17.
- [21] B. Wang, W. Ruan, J. Liu, T. Zhang, H. Yang, J. Ruan, Microstructure, mechanical properties, and preliminary biocompatibility evaluation of binary Ti–Zr alloys for dental application, *J. Biomater. Appl.* 33 (2019) 766–775, <https://doi.org/10.1177/0885328218811052>.
- [22] M.K. Han, M.J. Hwang, M.S. Yang, H.S. Yang, H.J. Song, Y.J. Park, Effect of zirconium content on the microstructure, physical properties and corrosion behavior of Ti alloys, *Mater. Sci. Eng.* 616 (2014) 268–274, <https://doi.org/10.1016/j.msea.2014.08.010>.
- [23] J. Jiang, C. Zhou, Y. Zhao, F. He, X. Wang, Development and properties of dental Ti–Zr binary alloys, *J. Mech. Behav. Biomed. Mater.* (2020), 104048, <https://doi.org/10.1016/j.jmbbm.2020.104048>.
- [24] T. Lee, T. Ueno, N. Nomura, N. Wakabayashi, T. Hanawa, Titanium-zirconium binary alloy as dental implant material: analysis of the influence of compositional change on mechanical properties and in vitro biologic response, *Int. J. Oral Maxillofac. Implants* (2016) 547–554, <https://doi.org/10.11607/jomi.4349>.

- [25] B. Yan, J. Tan, D. Wang, J. Qiu, X. Liu, Surface alloyed Ti–Zr layer constructed on titanium by Zr ion implantation for improving physicochemical and osteogenic properties, *Prog. Nat. Sci. Mater. Int.* 30 (2020) 635–641, <https://doi.org/10.1016/j.pnsc.2020.09.006>.
- [26] X. Zhao, M. Niinomi, M. Nakai, T. Ishimoto, T. Nakano, Development of high Zr-containing Ti-based alloys with low Young's modulus for use in removable implants, *Mater. Sci. Eng., C* 31 (2011) 1436–1444, <https://doi.org/10.1016/j.msec.2011.05.013>.
- [27] E. Kobayashi, M. Ando, Y. Tsutsumi, H. Doi, T. Yoneyama, M. Kobayashi, T. Hanawa, Inhibition effect of zirconium coating on calcium phosphate precipitation of titanium to avoid assimilation with bone, *Mater. Trans.* 48 (2007) 301–306, <https://doi.org/10.2320/matertrans.48.301>.
- [28] Y. Zhang, A.J. Davenport, B. Burke, N. Vyas, O. Addison, Effect of Zr addition on the corrosion of Ti in acidic and reactive oxygen species (ROS)-Containing environments, *ACS Biomater. Sci. Eng.* 4 (2018) 1103–1111, <https://doi.org/10.1021/acsbiomaterials.7b00882>.
- [29] I. Matula, G. Dercz, M. Zubko, J. Maszybrocka, J. Jurek-Suliga, S. Golba, I. Jendrzewska, Microstructure and porosity evolution of the ti–35zr biomedical alloy produced by elemental powder metallurgy, *Materials* 13 (2020) 1–14, <https://doi.org/10.3390/ma13204539>.
- [30] S.A. Naghavi, C. Lin, C. Sun, M. Tamaddon, M. Basiouny, P. Garcia-Souto, S. Taylor, J. Hua, D. Li, L. Wang, C. Liu, Stress shielding and bone resorption of press-fit polyether–ether–ketone (peek) hip prosthesis: a sawbone Model study, *Polymers* 14 (2022), <https://doi.org/10.3390/polym14214600>.
- [31] C. Ning, D. Ding, K. Dai, W. Zhai, L. Chen, The effect of Zr content on the microstructure, mechanical properties and cell attachment of Ti-35Nb-xZr alloys, *Biomed. Mater.* 5 (2010), <https://doi.org/10.1088/1748-6041/5/4/045006>.
- [32] J.S. Khashan, N.H. Rijja, T.A. Abbas, Modified polymer matrix nano biocomposite for bone repair and replacement- radiological study, *Eng. Technol. J.* 35 (2017) 365–371, <https://doi.org/10.30684/etj.35.4a.8>.
- [33] A. Sharma, J.N. Waddell, K.C. Li, L.A. Sharma, D.J. Prior, W.J. Duncan, Is titanium–zirconium alloy a better alternative to pure titanium for oral implant? Composition, mechanical properties, and microstructure analysis, *Saudi Dent. J.* 33 (2021) 546–553, <https://doi.org/10.1016/j.sdentj.2020.08.009>.
- [34] S. Piskunov, E. Heifets, R.I. Eglitis, G. Borstel, Bulk properties and electronic structure of SrTiO₃, BaTiO₃, PbTiO₃ perovskites: an ab initio HF/DFT study, *Comput. Mater. Sci.* 29 (2004) 165–178, [10.1016/j.commatsci.2003.08.036](https://doi.org/10.1016/j.commatsci.2003.08.036).
- [35] D. Khare, B. Basu, A.K. Dubey, Electrical stimulation and piezoelectric biomaterials for bone tissue engineering applications, *Biomaterials* 258 (2020), 120280, <https://doi.org/10.1016/j.biomaterials.2020.120280>.
- [36] M. Prakasam, M. Albino, E. Lebraud, M. Maglione, C. Elissalde, A. Largeau, Hydroxyapatite-barium titanate piezocomposites with enhanced electrical properties, *J. Am. Ceram. Soc.* 100 (2017) 2621–2631, <https://doi.org/10.1111/jace.14801>.
- [37] B. Amin, A. Shahzad, L. Farina, E. Parle, L. McNamara, M. O'Halloran, M.A. Elahi, Dielectric characterization of diseased human trabecular bones at microwave frequency, *Med. Eng. Phys.* 78 (2020) 21–28, <https://doi.org/10.1016/j.medengphy.2020.01.014>.
- [38] A. Das, V. Saxena, A. Bhardwaj, S. Rabha, L.M. Pandey, P. Dobbidi, Microstructural, interfacial, biological and electrical activity in sputtered Hydroxyapatite-Barium strontium titanate bilayered thin films, *Surface. Interfac.* 31 (2022), 102063, <https://doi.org/10.1016/j.surfint.2022.102063>.
- [39] T. Tariverdian, A. Behnamghader, P. Brouki Milan, H. Barzegar-Bafrooi, M. Mozafari, 3D-printed barium strontium titanate-based piezoelectric scaffolds for bone tissue engineering, *Ceram. Int.* 45 (2019) 14029–14038, <https://doi.org/10.1016/j.ceramint.2019.04.102>.
- [40] F.M. Ghorbani, B. Kaffashi, P. Shokrollahi, S. Akhlaghi, M.S. Hedenqvist, Effect of hydroxyapatite nano-particles on morphology, rheology and thermal behavior of poly(caprolactone)/chitosan blends, *Mater. Sci. Eng., C* 59 (2016) 980–989, <https://doi.org/10.1016/j.msec.2015.10.076>.
- [41] J. Yin, L. Xu, Batch preparation of electrospun polycaprolactone/chitosan/alginate blended nanofiber membranes for novel wound dressing, *Int. J. Biol. Macromol.* 160 (2020) 352–363, <https://doi.org/10.1016/j.ijbiomac.2020.05.211>.
- [42] E. Bolaina-Lorenzo, C. Martinez-Ramos, M. Monleón-Pradas, W. Herrera-Kao, J.V. Cauch-Rodríguez, J.M. Cervantes-Uc, Electrospun polycaprolactone/chitosan scaffolds for nerve tissue engineering: physicochemical characterization and Schwann cell biocompatibility, *Biomed. Mater.* 12 (2017), <https://doi.org/10.1088/1748-605X/12/1/015008>.
- [43] D.A. Salinas, C.L. Marchena, L.B. Pierella, G. Pecchi, Catalytic oxidation of 2-(methylthio)-benzothiazole on alkaline earth titanates, ATiO₃ (A = Ca, Sr, Ba), *Mol. Catal.* 438 (2017) 76–85, <https://doi.org/10.1016/j.mcat.2017.05.019>.
- [44] Q. Zhang, X. Li, Z. Ren, G. Han, C. Mao, Synthesis of CaTiO₃ nanofibers with controllable drug-release kinetics, *Eur. J. Inorg. Chem.* 2015 (2015) 4532–4538, <https://doi.org/10.1002/ejic.201500737>.
- [45] R. El Bahi, M. Dammak, W. Donner, A. Njeh, Charge compensation assisted enhancement of photoluminescence in (Li⁺, Mg²⁺, Sr²⁺) doped CaTiO₃: Eu/Dy/xGd for WLEDs applications, *J. Lumin.* 237 (2021), 118176, <https://doi.org/10.1016/j.jlumin.2021.118176>.
- [46] L.M. Angelats-Silva, F. Pérez-Azahuanche, J.A. Roldan-Lopez, N.A. Emelianov, R.B. Céspedes-Vásquez, M.A. Valverde-Alva, Influence of the surface modification of BaTiO₃ nanoparticles by hydrolyzed chitosan obtained from shrimp exoskeletons on the optical response intensity of the second harmonic, *MRS Adv* 7 (2022) 260–264, <https://doi.org/10.1557/s43580-022-00278-3>.
- [47] S. Swain, C. Bowen, T. Rautray, Dual response of osteoblast activity and antibacterial properties of polarized strontium substituted hydroxyapatite–barium strontium titanate composites with controlled strontium substitution, *J. Biomed. Mater. Res., Part A* 109 (2021) 2027–2035, <https://doi.org/10.1002/jbm.a.37195>.
- [48] M. Prodana, C.E. Nistor, A.B. Stoian, D. Ionita, C. Burnei, Dual nanofibrous bioactive coatings on TiZr implants, *Coatings* 10 (2020) 1–16, <https://doi.org/10.3390/COATINGS10060526>.
- [49] K. Kalwar, W.X. Sun, D.L. Li, X.J. Zhang, D. Shan, Coaxial electrospinning of polycaprolactone@chitosan: characterization and silver nanoparticles incorporation for antibacterial activity, *React. Funct. Polym.* 107 (2016) 87–92, <https://doi.org/10.1016/j.reactfunctpolym.2016.08.010>.
- [50] L. Zhu, W. Gu, H. Li, W. Zou, H. Liu, Y. Zhang, Q. Wu, Z. Fu, Y. Lu, Enhancing the photocatalytic hydrogen production performance of SrTiO₃ by coating with a hydrophilic poloxamer, *Appl. Surf. Sci.* 528 (2020), 146837, <https://doi.org/10.1016/j.apsusc.2020.146837>.
- [51] L.M. Anaya-Esparza, J.M. Ruvalcaba-Gómez, C.I. Maytorena-Verdugo, N. González-Silva, R. Romero-Toledo, S. Aguilera-Aguirre, A. Pérez-Larios, E. Montalvo-González, Chitosan-tio₂: a versatile hybrid composite, *Materials* 13 (2020), <https://doi.org/10.3390/ma13040811>.
- [52] Y. Liu, Y. Liu, N. Liao, F. Cui, M. Park, H.Y. Kim, Fabrication and Durable Antibacterial Properties of Electrospun Chitosan Nanofibers with Silver Nanoparticles, *Elsevier B.V.*, 2015, <https://doi.org/10.1016/j.ijbiomac.2015.05.058>.
- [53] M. Sasikumar, A. Ganeshkumar, M.N. Chandraprabha, R. Rajaram, R.H. Krishna, N. Ananth, P. Sivakumar, Investigation of Antimicrobial activity of CTAB assisted hydrothermally derived Nano BaTiO₃, *Mater. Res. Express* 6 (2019), 25408, <https://doi.org/10.1088/2053-1591/aaec3b>.
- [54] A. Singh, A.K. Dubey, Improved antibacterial and cellular response of electrets and piezobioceramics, *J. Biomater. Appl.* 36 (2021) 441–459, <https://doi.org/10.1177/0885328221991965>.
- [55] L. Zhang, P.Y. Tan, C.L. Chow, C.K. Lim, O.K. Tan, M.S. Tse, C.C. Sze, Antibacterial activities of mechanochemically synthesized perovskite strontium titanate ferrite metal oxide, *Colloids Surfaces A Physicochem. Eng. Asp.* 456 (2014) 169–175, <https://doi.org/10.1016/j.colsurfa.2014.05.032>.
- [56] R. Liu, K. Memarzadeh, B. Chang, Y. Zhang, Z. Ma, R.P. Allaker, L. Ren, K. Yang, Antibacterial effect of copper-bearing titanium alloy (Ti-Cu) against *Streptococcus mutans* and *Porphyromonas gingivalis*, *Sci. Rep.* 6 (2016) 1–10, <https://doi.org/10.1038/srep29985>.
- [57] J. Luo, S. Guo, Y. Lu, X. Xu, C. Zhao, S. Wu, J. Lin, Cytocompatibility of Cu-bearing Ti6Al4V alloys manufactured by selective laser melting, *Mater. Char.* 143 (2018) 127–136, <https://doi.org/10.1016/j.matchar.2017.12.003>.
- [58] B. Wang, A. Bian, F. Jia, J. Lan, H. Yang, K. Yan, L. Xie, H. Qiao, X. Chang, H. Lin, H. Zhang, Y. Huang, “Dual-functional” strontium titanate nanotubes designed based on fusion peptides simultaneously enhancing anti-infection and osseointegration, *Biomater. Adv.* 133 (2022), 112650, <https://doi.org/10.1016/j.msec.2022.112650>.
- [59] H. Chang, H. Xiang, Z. Yao, S. Yang, M. Tu, X. Zhang, B. Yu, Strontium-substituted calcium sulfate hemihydrate/hydroxyapatite scaffold enhances bone regeneration by recruiting bone mesenchymal stromal cells, *J. Biomater. Appl.* 35 (2020) 97–107, <https://doi.org/10.1177/0885328220915816>.